

Negative Differential Resistance and Steep Switching in Chevron Graphene Nanoribbon Field Effect Transistors

Samuel Smith, Juan-Pablo Llinás, Jeffrey Bokor, Sayeef Salahuddin¹

University of California, Berkeley, Department of Electrical Engineering and Computer Sciences, Berkeley, CA 94720

Ballistic quantum transport calculations based on the non-equilibrium Green's function formalism show that field-effect transistor devices made from chevron-type graphene nanoribbons (CGNRs) could exhibit negative differential resistance with peak-to-valley ratios in excess of 4800 at room temperature as well as steep-slope switching with 6 mV/decade subthreshold swing over five orders of magnitude and ON-currents of $88 \mu\text{A } \mu\text{m}^{-1}$. This is enabled by the superlattice-like structure of these ribbons that have large periodic unit cells with regions of different effective bandgap, resulting in minibands and gaps in the density of states above the conduction band edge. The CGNR ribbon used in our proposed device has been previously fabricated with bottom-up chemical synthesis techniques and could be incorporated into an experimentally-realizable structure.

In 1970, L. Esaki and R. Tsu predicted¹ that in an appropriately made superlattice, it should be possible to obtain very narrow width bands, which could then lead to negative differential resistance. The remarkable property of these superlattices is in the fact that, unlike the Esaki diodes, this negative differential resistance does not need any tunneling, rather it comes from the direct conduction of electrons. Nonetheless, significant difficulty in synthesizing atomically precise, epitaxial heterostructures has made it very challenging to realize such superlattice structures²⁻⁸. Much work has been done on modeling graphene nanoribbon heterostructures and superlattices which could exhibit NDR⁹⁻¹⁵. Other work has been done on steep slope devices based on GNR and CNT heterojunctions^{16,17}. Gnani *et al.* showed how superlattices could be used in a III-V nanowire FET to achieve steep slope behavior by using the superlattice gap to filter high energy electrons in the OFF state¹⁸. Here, we show that the recently synthesized chevron nanoribbons¹⁹ provides a natural, monolithic material system where narrow-width energy bands and negative differential resistance (NDR) can be achieved. Our atomistic calculations predict that the NDR behavior should manifest at room temperature along with sub-thermal steepness (<60 mV/decade at room temperature). Such NDR behavior could lead to completely novel devices for next generation electronics.

Unlike a graphene sheet, a narrow strip etched out of graphene, often called a graphene nanoribbon (GNR), can provide a sizeable bandgap. As a result, GNRs could lead to devices with good ON/OFF ratio at the nanoscale. However, a number of studies have also shown the deleterious effect of edge roughness on the device performance^{20,21}. Recent breakthroughs in bottom-up chemical synthesis can produce GNRs with atomistically pristine edge states and overcome this shortcoming¹⁹. In fact, a recent experimental work demonstrated working transistors with 9- and 13-AGNRs made with these techniques²². The methods used to synthesize these ribbons can also be used to generate complex periodic structures beyond simply armchair and zigzag nanoribbons^{23,24}. In this work, we will consider one

of those structures, the chevron graphene nanoribbon (CGNR).

Fig. 1 shows both the atomic structure of the 6-9 CGNR originally fabricated by Cai *et al.* and the electronic structure calculated through a p_z orbital-based tight-binding method¹⁹. A key feature of the band structure is the presence of minibands with regions of forbidden energy above the conduction band edge, such as those seen in superlattices of III-V semiconductors. Analogous to III-V superlattices, the CGNR contains regions of different effective bandgap. When we look at the CGNR in Fig. 1, we see that its narrowest segment is 6 carbon atoms across and its widest segment is 9 carbon atoms across, with both segments having armchair-type edges. Using a p_z -basis set (GW²⁵), the bandgap, E_g , of a 6-AGNR is 1.33 eV (2.7 eV) and the bandgap of a 9-AGNR is 0.95 eV (2.0 eV). However, given the very short length scale over which the width changes in our structure (~ 1 nm), one would not expect the system to behave as though the local effective potential oscillates between the bulk values of E_g for the isolated AGNRs. In fact, our chevron structure has an overall bandgap of 1.59 eV. This value is consistent with the 1.62 eV bandgap from LDA DFT calculations, but significantly smaller than the 3.74 eV value from calculations incorporating the GW correction²⁶. Both LDA and GW calculations show the presence of minibands and gaps above the conduction band edge²⁶.

The structure of the simulated device is shown in in Fig. 2. Like a typical MOSFET, our superlattice field-effect transistor (SLFET) can be turned ON and OFF with a gate voltage at low drain biases. Operation differs from a MOSFET in two key ways. The first is that the device shows NDR with respect to the drain voltage. At some value of V_{ds} determined by the width of the first miniband, I_d decreases substantially when the conduction band at the source becomes aligned with the superlattice gap at the drain. At higher drain bias, current increases again when the conduction band at the source is aligned with the second miniband at the drain. The second feature of the SLFET is that the superlattice gap at the drain filters out higher energy electrons

from the first miniband at the source when a source-drain bias is applied. This cuts off the higher energy portion of the thermionic tail at the source, which would contribute to leakage current in a traditional MOSFET. This filtering does not, however, affect the low-energy electrons, which carry most of the ON state current as they are in the window where the first minibands at the source and drain overlap. Transport in an SLFET is entirely intra-band like a MOSFET, whereas a TFET relies on band-to-band tunneling. This could possibly allow higher ON current than a TFET.

The CGNR used in our simulation has a width of 1.9 nm. The simulation domain is approximately 70 nm long, and the gate has a length of 15 nm. The source and drain are doped with $N_D = 1.0 \times 10^{13} \text{ cm}^{-2}$ donors. An effective oxide thickness of 1.0 nm is used for both the top and bottom gates. The gate contacts are extended 30 nm in the direction perpendicular the channel to capture the effects of fringing gate fields. While our simulation uses an effective doping density to align the source and drain Fermi levels to the CGNR conduction band, the same effect could be achieved in an experiment through electrostatics alone.

Simulations are performed using the non-equilibrium Greens function (NEGF) formalism²⁷. A simple p_z -basis is used for the Hamiltonian for the chevron graphene nanoribbon with the hopping parameter set to $t_0 = 2.7 \text{ eV}$. Charge and current are calculated with the recursive Greens function algorithm²⁸, and contact self-energy is computed with the Sancho-Rubio iteration scheme²⁹.

The NEGF equations are solved self-consistently with

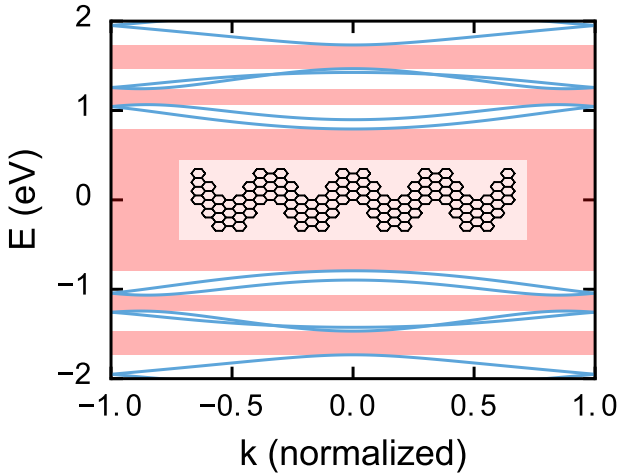


FIG. 1. Band structure of a chevron graphene nanoribbon based on a p_z orbital basis set. The width (and thus quantum confinement) varies across the unit cell, giving a superlattice-like band structure. Forbidden energies are highlighted in red. The bandgap of the ribbon is 1.59 eV, the first conduction band has a bandwidth of 0.272 eV, and the first gap between minibands is 0.178 eV. Inset: Molecular structure of the chevron nanoribbon.

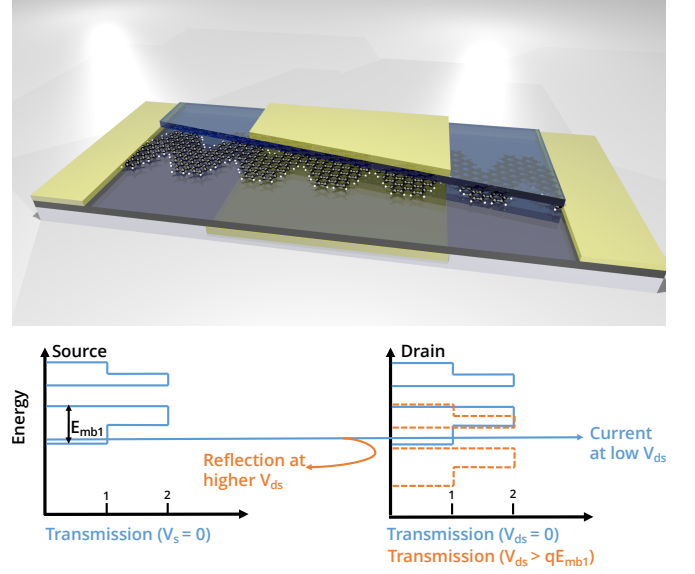


FIG. 2. Artistic rendering of double-gate CGNR on insulator SLFET. Parts of the top gate and oxide region have been cut away so that the channel is visible. When a gate voltage is applied to turn the device ON, current conduction occurs at low values of V_{ds} where the first miniband at the source is aligned with the first miniband at the drain. As the drain voltage is increased beyond qE_{mb1} , the bandwidth of the first miniband, transmission from source to drain is cut off and the device exhibits negative differential resistance.

the Poisson equation for electrostatics in three dimensions. Our simulator solves the nonlinear Poisson equation using the predictor-corrector scheme described by Trellakis *et al.* using a semiclassical approximation for the charge density³⁰. The geometry of the system is modeled using a tetrahedral finite element mesh generated with the SALOME package³¹. The solution of the final sparse matrix form of the Poisson equation discretized with the finite element method is performed using the conjugate gradient solver from the Eigen library³².

The local density of states for the CGNR MOSFET is shown in Fig. 3 for several biasing conditions. Fig. 3b shows the case for peak current for the device when a large enough drain bias has been applied to generate enough splitting between the source and drain Fermi levels to allow significant current to flow, but not a high enough bias to move the the first miniband outside of the current conduction window. For higher bias as in Fig. 3c, intraband conduction from the first miniband is completely cut off. As the drain bias is further increased, current can only flow due to a band-to-band tunneling from the first miniband at the source to the second miniband at the drain. Note that, due to the minibands, there will be regions of operation for both gate and drain voltages where current flow is abruptly turned on or off, as the overlap between source minibands and drain minibands is modified. This leads to a steep subthreshold swing ($< 60 \text{ mV/decade}$ at room temperature) in the $I_d - V_g$

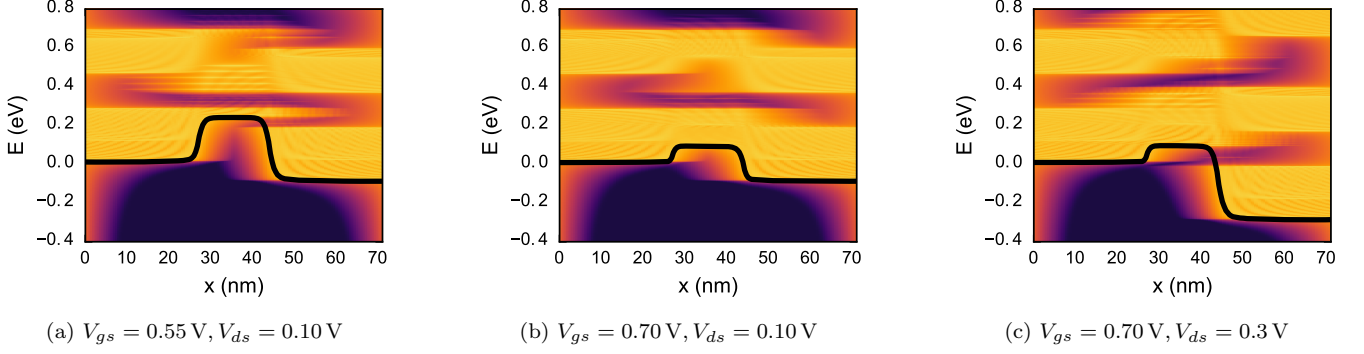


FIG. 3. Local density of states for several different biasing conditions. Fig. (a) shows the OFF state, in which leakage current is substantially reduced because the superlattice gap in the drain region filters higher energy electrons, which could otherwise travel over the source-side barrier. Fig. (b) shows the ON state, in which current is primarily carried by lower energy carriers, which are not blocked through the density of states filtering at the drain. Fig. (c) shows the ON state for a higher value of V_{ds} . Significant ballistic transport from source to drain is no longer possible when the drain voltage is greater than the width of the first miniband minus the height of the source-side barrier. The colormap is based on a logarithmic scale.

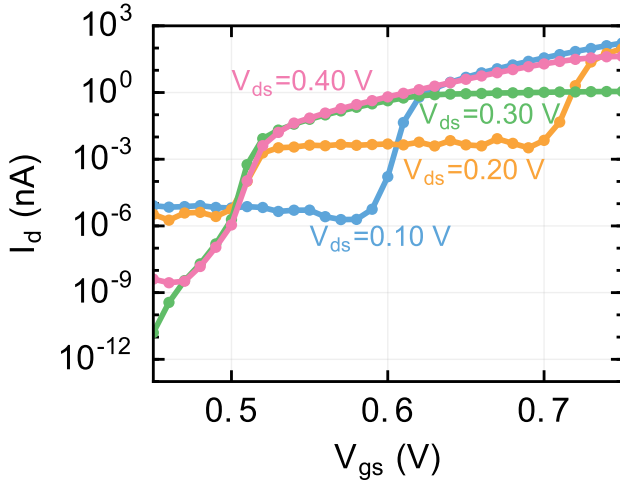


FIG. 4. $I_d - V_{gs}$ plot for different values of V_{ds} . Steep-slope behavior is observed with a subthreshold swing of around 6 mV/decade over five orders of magnitude around $V_{gs} = 0.6$ V for the case when $V_{ds} = 0.1$ V. Negative differential resistance is evident in that the peak value of I_d is lower for higher values of V_{ds} .

characteristic and a negative differential resistance in the $I_d - V_d$ characteristic.

We shall first discuss the current vs gate voltage ($I_d - V_g$) characteristics. Fig. 4 shows I_d vs. V_{gs} for several values of V_{ds} . While steep slope behavior is exhibited at some point for all values of V_{ds} , the highest ON current is observed for $V_{ds} = 0.1$ V. At this drain bias, an ON current of 168 nA ($88 \mu\text{A} \mu\text{m}^{-1}$) is achieved at a gate bias of $V_{gs} = 0.75$ V. In the steep slope region of this curve, the subthreshold swing is 6 mV/decade when averaged over five orders of magnitude of I_d . With gate work function engineering and additional device optimization,

it should be possible to achieve reasonable ON current with a low supply voltage in devices of this type. The origin of the steep-slope behavior can be understood from Fig. 3. In the OFF state shown in Fig. 3a, the superlattice gap at the drain prevents leakage current from flowing over the source-side injection barrier. The states near the top of the barrier are seen to decay rapidly in the drain region. Fig. 3b shows the ON state, in which low-energy electrons, which make up virtually all of the ON current, can flow unimpeded from source to drain.

The $I_d - V_{ds}$ curves from the results of our simulation are shown in Fig. 5. Considering the case when $V_{gs} = 0.7$ V, we see an increase in current up to $V_{ds} = 0.10$ V. As the drain bias is further increased, we see a decrease in current as the drain miniband goes out of alignment with the source miniband. The current begins to pick up again as the second miniband at the drain starts to come in alignment with the source miniband again. The peak-to-valley ratio (PVR) at this gate voltage is 4.88×10^3 . At $V_{gs} = 0.60$ V, the calculated PVR is 1.71×10^8 . Note, however, that this value is expected to be much smaller in a practical device due to the electron-phonon scattering mechanisms²⁸ that were not taken into account in our ballistic simulations.

In summary, we have shown that chevron graphene nanoribbon devices can exhibit both steep-slope subthreshold behavior and negative differential resistance. Both properties are the result of the superlattice-like electronic structure of the ribbon. CGNR SLFETs could be promising for a number of applications ranging from low-power logic transistors to high speed oscillators. A major obstacle to building a real device is making contacts with appropriate Schottky barrier heights to be able to match the band alignment conditions achieved in this work through a simple doping model. The performance of a real device would also likely be impacted by scattering mechanisms we have not considered here,

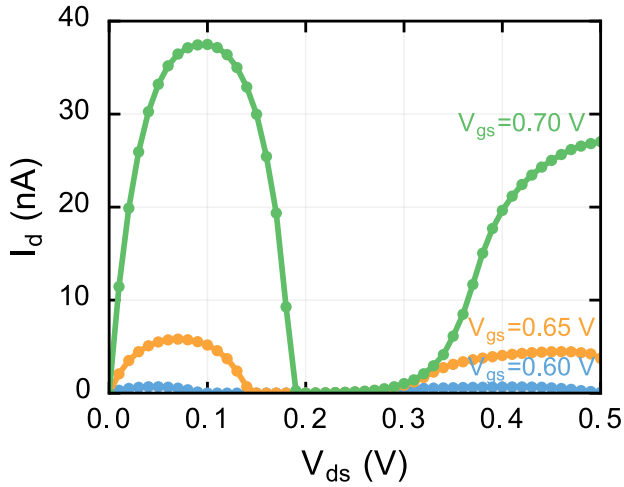


FIG. 5. $I_d - V_{ds}$ plot for different values of V_{gs} . For the case, when $V_{gs} = 0.7$ V, a peak-to-valley ratio of 4.88×10^3 is achieved.

though the ability to synthesize ribbons with virtually no defects may minimize these effects. Additional optimization will also likely be necessary to make a functioning device. DFT+GW calculations predict a much higher bandgap for the CGNR in vacuum than the tight-binding model used in this work. While surface screening may reduce the bandgap somewhat, a wider ribbon with a narrower bandgap may be required. Co-optimization of the bandgap with the bandwidths of the minibands and the gaps between minibands is also a necessary topic for future work.

ACKNOWLEDGEMENTS

This work was supported by NSF CAREER grant CISE-1149804. Work by JPL and JB was supported in part by the Office of Naval Research BRC program under Grant N00014-16-1-2229. The authors would like to acknowledge useful discussions with Felix Fischer and Michael Crommie.

- ¹L. Esaki and R. Tsu, IBM Journal of Research and Development **14**, 61 (1970).
- ²L. Esaki and L. Chang, Physical Review Letters **33**, 495 (1974).
- ³K. Choi, B. Levine, R. Malik, J. Walker, and C. Bethea, Physical Review B **35**, 4172 (1987).
- ⁴K. Ismail, W. Chu, A. Yen, D. Antoniadis, and H. I. Smith, Applied physics letters **54**, 460 (1989).

- ⁵G. Bernstein and D. Ferry, Journal of Vacuum Science & Technology B: Microelectronics Processing and Phenomena **5**, 964 (1987).
- ⁶H. Grahm, R. Haug, W. Müller, and K. Ploog, Physical review letters **67**, 1618 (1991).
- ⁷J. Kastrup, H. Grahm, K. Ploog, F. Prengel, A. Wacker, and E. Schöll, Applied physics letters **65**, 1808 (1994).
- ⁸A. Warren, D. Antoniadis, H. I. Smith, and J. Melngailis, IEEE electron device letters **6**, 294 (1985).
- ⁹G. J. Ferreira, M. N. Leuenberger, D. Loss, and J. C. Egues, Physical Review B **84**, 125453 (2011).
- ¹⁰S. Li, C. K. Gan, Y.-W. Son, Y. P. Feng, and S. Y. Quek, Applied Physics Letters **106**, 013302 (2015).
- ¹¹H. Teong, K.-T. Lam, S. B. Khalid, and G. Liang, Journal of Applied Physics **105**, 084317 (2009).
- ¹²H. Sevinçli, M. Topsakal, and S. Ciraci, Physical Review B **78**, 245402 (2008).
- ¹³M. Sharifi, E. Akhondi, and H. Esmaili, Journal of Computational Electronics, 1 (2016).
- ¹⁴G. Saha, A. K. Saha, and A. H.-u. Rashid, in *Nanotechnology (IEEE-NANO), 2015 IEEE 15th International Conference on* (IEEE, 2015) pp. 440–443.
- ¹⁵E. C. Girao, E. Cruz-Silva, and V. Meunier, ACS nano **6**, 6483 (2012).
- ¹⁶S. Kim, M. Luisier, T. B. Boykin, and G. Klimeck, Applied Physics Letters **104**, 243113 (2014).
- ¹⁷Y. Yoon and S. Salahuddin, Applied Physics Letters **97**, 033102 (2010).
- ¹⁸E. Gnani, P. Maiorano, S. Reggiani, A. Gnudi, and G. Baccarani, in *Electron Devices Meeting (IEDM), 2011 IEEE International* (IEEE, 2011) pp. 5–1.
- ¹⁹J. Cai, P. Ruffieux, R. Jaafar, M. Bieri, T. Braun, S. Blankenburg, M. Muoth, A. P. Seitsonen, M. Saleh, X. Feng, K. Müllen, and R. Fasel, Nature **466**, 470 (2010).
- ²⁰G. Fiori and G. Iannaccone, IEEE Electron Device Letters **28**, 760 (2007).
- ²¹Y. Yoon and J. Guo, Applied Physics Letters **91**, 073103 (2007).
- ²²J. P. Llinás, A. Fairbrother, G. Barin, P. Ruffieux, W. Shi, K. Lee, B. Y. Choi, R. Braganza, N. Kau, W. Choi, Z. Pedramrazi, T. Dumsclaff, A. Narita, X. Feng, K. Müllen, F. Fischer, A. Zettl, P. Ruffieux, E. Yablonovitch, M. Crommie, R. Fasel, and J. Bokor, arXiv preprint arXiv:1605.06730 (2016).
- ²³J. Cai, C. A. Pignedoli, L. Talirz, P. Ruffieux, H. Söde, L. Liang, V. Meunier, R. Berger, R. Li, X. Feng, K. Müllen, and R. Fasel, Nature nanotechnology **9**, 896 (2014).
- ²⁴Y.-C. Chen, T. Cao, C. Chen, Z. Pedramrazi, D. Haberer, D. G. de Oteyza, F. R. Fischer, S. G. Louie, and M. F. Crommie, Nature nanotechnology **10**, 156 (2015).
- ²⁵L. Yang, C.-H. Park, Y.-W. Son, M. L. Cohen, and S. G. Louie, Physical Review Letters **99**, 186801 (2007).
- ²⁶S. Wang and J. Wang, The Journal of Physical Chemistry C **116**, 10193 (2012).
- ²⁷S. Datta, *Quantum transport: atom to transistor* (Cambridge University Press, 2005).
- ²⁸R. Lake, G. Klimeck, R. C. Bowen, and D. Jovanovic, Journal of Applied Physics **81**, 7845 (1997).
- ²⁹M. L. Sancho, J. L. Sancho, J. L. Sancho, and J. Rubio, Journal of Physics F: Metal Physics **15**, 851 (1985).
- ³⁰A. Trellakis, A. Galick, A. Pacelli, and U. Ravaioli, Journal of Applied Physics **81**, 7880 (1997).
- ³¹A. Ribes and C. Caremoli, in *Computer Software and Applications Conference, 2007. COMPSAC 2007. 31st Annual International*, Vol. 2 (IEEE, 2007) pp. 553–564.
- ³²G. Guennebaud and B. Jacob, “Eigen v3,” <http://eigen.tuxfamily.org> (2010).